# Tuning Two-Dimensional Phthalocyanine Dual Site Metal Organic Framework Catalysts for the Oxygen Reduction Reaction

*Lingze Wei[1,2‡], Md Delowar Hossain[1,2‡], Gan Chen[3‡], Gaurav A. Kamat[1,2], Melissa E. Kreider[1,2], Junjie Chen[1,2], Katherine Yan[1,2], Zhenan Bao[1,2], Michal Bajdich[2*], Michaela Burke Stevens[2*], Thomas F. Jaramillo[1,2*]*

[1]Department of Chemical Engineering, Stanford University, Stanford, CA, USA, 94305

[2]SUNCAT Center for Interface Science and Catalysis, SLAC National Accelerator Laboratory, Menlo Park, CA, USA, 94025

[3]Department of Materials Science and Engineering, Stanford University, Stanford, CA, USA, 94305

[‡]These authors contributed equally

[*]Corresponding Authors: bajdich@slac.stanford.edu, mburkes@slac.stanford.edu, jaramillo@stanford.edu

Keywords: Oxygen Reduction Reaction, Electrocatalysis, Metal Organic Framework, Single-Atom Catalysts, Computational Catalysis, Electrochemical Stability.

## Abstract

Metal-organic frameworks (MOFs) offer an interesting opportunity for catalysis, particularly for metal-nitrogen-carbon (M-N-C) motifs by providing an organized porous structural pattern and well-defined active sites for the oxygen reduction reaction (ORR), a key need for hydrogen fuel cells and related sustainable energy technologies. In this work, we leverage electrochemical testing with computational models to study the electronic and structural properties in these systems and their relationship to ORR activity and stability based on dual transitional metal centers. These consists of two M1 metals with amine nodes coordinated to a single M2 metal with a phthalocyanine linker, where M1/M2 = Co, Ni, or Cu. Co-based metal centers, in particular Ni-Co, demonstrate the highest overall activity of all nine tested MOFs. Computationally, we identify the dominance of Co-sites, relative higher importance of the M2 site, and the role of layer M1 interactions on the ORR activity. Selectivity measurements indicate that M1 sites of MOFs, particularly Co, exhibits lowest (< 4%), and Ni demonstrates highest (>46%) two-electron selectivity, in good agreement with computational studies. Direct *in-situ* stability characterization, measuring dissolved metal ions, and calculations, using an alkaline stability metric, confirm that Co is the most stable metal in the MOF, while Cu exhibits notable instability at the M1. Overall, this study reveals how atomistic coupling of electronic and structural properties affects the ORR performance of dual site MOF catalysts and opens new avenues for tunable design and future development of these systems for practical electrochemical applications.

# 1. Introduction

Hydrogen fuel cells have been gaining traction in energy and sustainability domains to meet the energy demand as well as address global climate change.[1–4] In fuel cells, hydrogen is oxidized (hydrogen oxidation reaction, HOR) and oxygen is reduced (oxygen reduction reaction, ORR) electrochemically to convert the energy stored in chemical bonds to electrical energy that could supply a growing number of green and sustainable electrified systems.[3] However, the sluggish kinetics and the large overpotential required for the ORR at the cathode severely limit the energy conversion efficiency, hindering the at-scale production of hydrogen fuel cell devices.[2,5,6] Alkaline fuel cells present a promising direction for low-cost energy conversion as the alkaline environment opens doors for utilizing a wide variety of earth-abundant non-noble metal catalysts.[5] Development of efficient non-noble ORR catalysts with improved reaction kinetics, selectivity and durability in alkaline electrolytes is essential in promoting fuel cell applications towards a sustainable future.

Depending on the nature of the catalyst, the ORR proceeds either via a direct four-electron pathway or a partial two-electron pathway as follows (in alkaline media):[7–9]

$$4e^- ORR\ (E_o = 1.23\ V\ vs. RHE):$$

$$O_2 + 2H_2O + 4e^- \rightarrow 4OH^- \qquad (1)$$

$$2e^- ORR\ (E_o = 0.70\ V\ vs. RHE):$$

$$O_2 + H_2O + 2e^- \rightarrow HO_2^- + OH^- \qquad (2)$$

Overall, theoretical calculations based on density functional theory (DFT) have been used to complement experimental activity measurements by predicting the thermodynamics and kinetics of ORR reactions (**Equations 1, 2**).[10] The reaction free energy of the OH* intermediate is typically considered the main descriptor to evaluate catalytic activity and selectivity for ORR. Although it is challenging to predict the two vs. four-electron pathways only from OH*, on weak-binding surfaces ORR is typically thought to proceed *via* the two-electron pathway rather than the four-electron pathway due to the difficult nature of breaking the O-O bond.[7] Kulkarni et al. showed that for an ORR Volcano plot, metals that bind *OH strongly on the left side of the volcano have

increased four-electron selectivity as the $*OH \rightarrow H_2O$ step is the rate limiting step; whereas on the right side, metals weakly bind the adsorbates, resulting in $O_2 \rightarrow *OOH$ as the potential limiting step resulting in increased two-electron selectivity.[7] Recently, Kelly et al. predicted that weak *OOH binding surfaces, such as Au(100), are strongly influenced by the external electric field originating from an increasing pH which subsequently enhanced the four-electron ORR activity without affecting the two-electron ORR activity.[8]

First-row transition metals, when incorporated into the metal-nitrogen-carbons (M-N-Cs) matrix, have demonstrated promising four-electron ORR selectivity with robust kinetics.[11–14] However, the M-N-C synthesis method, e.g., pyrolysis, can create multiple active centers that are difficult to characterize and to control. Transition metal-based metal-organic frameworks (MOFs), a sub-class of the M-N-Cs and often used as the precursors for pyrolyzed M-N-Cs, are of particular of interest as their organized structural pattern allows for control over the metal dispersion.[15–18] Moreover, their high porosity and large surface area from the structured pores could theoretically enable enhanced mass transport to accessible single-site active centers, facilitating a higher total turnover during electrochemistry.[19–22] One type of MOF active center, the M-$N_4$ moiety, which resembles the metalloprotein structure found commonly in living systems that facilitate similar reactions, has been widely recognized for its ORR activity and four-electron selectivity.[11,15,22,23] Recent works indicate that by altering the metal center and its coordination with nitrogen, it is possible to modify the electronic structure, adjust the $M^{2+/3+}$ redox potential, optimize the kinetics of the ORR, and influence oxygen reduction mechanisms.[24,25] Previous computational studies have also shown that isolated M-$N_4$ sites follow the same scaling relations for O*, *OH, *OOH as metal surfaces.[26,27] However, in MOF systems, two different M-$N_4$ sites can be altered independently or together, which can possibly develop internal stress or strain within the structure and modify the electronic and structural properties, and can ultimately affect the ORR activity, selectivity, and durability.

In order to understand relationships between the highly ordered, well-defined active sites and their ORR performance, the structural stability of MOFs under (electro)chemical operation is of critical importance. At the forefront of this interest is determining whether the MOF is a pre-catalyst or catalyst during electrocatalysis. In

this context, the MOF as a pre-catalyst would mean that the MOF catalyst is synthesized, but converted substantially into a new operating catalyst either prior to electrochemical treatment (e.g., thermal treatment) or during electrochemical operation. A MOF catalyst, however, implies that the coordinate bonding between the metal and the organic ligand as well as the pore structure is largely maintained during operation. This metal-organic bond is generally considered weaker than the ionic and/or covalent bonding present in other electrocatalysts.[28] Moreover, the use of various 3d- transition metals as metal centers for mixed MOF systems can develop internal strain or stress due to the size difference, layer stacking, and the nature of bonding with organic ligands. Hence, a structural transformation (e.g., framework dissociation, metal agglomeration, etc.) can take place in the (electro)chemical environment over time, making it difficult to establish structure-performance relationships.[28] Therefore, direct *in-situ* stability studies are crucial in determining the structural evolution of MOFs under electrocatalytic operating conditions while establishing activity-stability relationships.

In this work, we synthesized 2D phthalocyanine-MOF-based catalysts with dual M-$N_4$ sites (M1/M2 = Co, Ni, Cu, M1 = amine coordinated node and M2 = phthalocyanine center) and explore their potential in alkaline fuel cell applications both experimentally and computationally. These catalysts have greater structural stability in alkaline media and present higher crystallinity when constructed with Co, Ni, or Cu. Alternative to traditional M-N-Cs, by strategically tuning the choice and placement of metals, we can modify the electronic and geometric properties of the MOFs to investigate the M1-M2 interaction and correlate the electrochemical performance with an ordered material structure. We conducted electrochemical measurements to establish the ORR performance as a function of metal site composition. MOF surface layer models with ORR active sites were used for thermodynamic ORR activity and stability DFT calculations, with dissolution computed explicitly under alkaline electrochemical ORR conditions. *Ex-situ* spectroscopy was coupled to *in-situ* mass spectrometry to obtain information on MOF changes in metal oxidation states, local coordination environment, and preferential metal dissolution during electrochemistry. Finally, we discuss the correlation between dual metal sites and shed light on the activity and stability of the metal sites within the MOFs during ORR with possible structural degradation

pathways. This integrated approach, combining electrochemistry and thorough material characterization with theoretical analysis, establishes a robust platform for investigating MOF-based electrocatalysts.

## 2. Methods

### 2.1 Materials

All materials were used as received unless otherwise noted: Isopropyl alcohol (Sigma Aldrich, anhydrous ≥ 99.5 %), Nafion 117 containing solution (Sigma Aldrich, ~5% in lower aliphatic alcohols and water), potassium hydroxide (Sigma Aldrich, semiconductor grade pellets), Vulcan carbon (XC 72, Fuel Cell Store), Co Standard for ICP (Fluka Analytical, 1,000 mg $L^{-1}$ ± 2 mg $L^{-1}$ Co in $HNO_3$), Ni Standard for ICP (Sigma Aldrich, 1,000 mg $L^{-1}$ ± 2 mg $L^{-1}$ Ni in $HNO_3$), Cu Standard for ICP (Fluka Analytical, 1,001 mg $L^{-1}$ ± 2 mg $L^{-1}$ Cu in $HNO_3$), glassy carbon working electrodes (area = 0.196 $cm^2$, HTW Hochtemperatur-Werkstoffe GmbH, polished), graphite counter electrode (Ted Pella), Ag/AgCl reference electrode (Fisherbrand, Accumet).

### 2.2 Synthesis

All the phthalocyanine-based MOFs were prepared following our reported procedures.[29] Briefly, the home-made metal (II) 2,3,9,10,16,17,23,24-octaamino-phthalocyanine ligands (5 mg, 5 μmol) was dispersed in 3.5 mL dimethylformamide (DMF) or dimethylacetamide (DMA). The corresponding transition metal ($Co^{2+}$/$Ni^{2+}$/$Cu^{2+}$, 15 μmol) nitrates was then dissolved in 0.75 mL sodium acetate (NaOAc) aqueous solution (1.6 M) and 1.5 mL DMF or DMA and added into the ligand solution. The mixture was further heated in air under stirring for 4h and filtered to give the MOF powders.

### 2.3 Ex-Situ Physical Characterization

X-ray photoelectron spectroscopy (XPS) was performed using a Phi Versaprobe 3 with monochromatized Al Kα (1486.4 eV) radiation. The spectra were calibrated to the

adventitious C 1s peak at 284.8 eV. Using CasaXPS software,[30] peak fitting was performed with Shirley backgrounds and Gaussian-Lorentzian line shapes. Transmission electron microscopy (TEM) images of spent MOF materials were collected on an FEI Tecnai G2 F20 X-TWIN transmission electron microscope at 200 kV accelerating voltage with a Gatan ORIUS SC200 CCD camera.

### 2.4 Electrochemical Characterization

Electrochemical measurements were performed in 0.1 M KOH solution (Sigma-Aldrich, semiconductor grade) purged with $O_2$ or Ar (Research Grade 5.0, Praxair) in a rotating disk electrode (RDE) or rotating ring disk electrode (RRDE) setup. A graphite rod (Ted Pella) was used as the counter electrode and an Ag/AgCl electrode (Accumet) was used as the reference. The Ag/AgCl reference electrode was calibrated using a Pt wire as the working electrode in a $H_2$-saturated electrolyte, and a value of ~0.951 V to the reversible hydrogen electrode (RHE) scale was obtained. 85% of the iR losses were compensated during the measurements for RDE, RRDE and flow cell online ICP-MS measurements[31] (see **Section 2.5**) using a Biologic VSP-300 Potentiostat.

The working electrode ink was prepared by mixing 1 mg of catalyst, 0.5 mg of Vulcan carbon, 100 µL of isopropyl alcohol ($\rho$ = 0.785 g $mL^{-1}$ at 25°C), 50 µL of DI water and 2.3 µL 5% Nafion 117 solution ($\rho$ = 0.874 g $mL^{-1}$ at 25°C). 10 µL of the resulting catalyst ink was drop-casted onto a clean and polished glassy carbon (GC) disk followed by spinning at 400 rpm to obtain a final catalyst loading of 0.33 mg $cm^{-2}$.

RDE electrochemical measurements were carried out by sweeping the disk potential between 0 V and 1.1 V vs. RHE at 20 mV/s unless otherwise specified. The ORR activity was determined by subtracting the current obtained in an Ar-saturated electrolyte from that obtained in an $O_2$-saturated electrolyte ($j_{O2}$ - $j_{Ar}$). RRDE measurements were carried out using the same RDE disk parameters while holding the Au ring at 1.23 V vs. RHE to oxidize $H_2O_2$ species formed on the disk electrode, quantifying ORR products. The system's ring collection efficiency (N) was determined to be 0.2245 using the reversible $[Fe(CN)_6]^{4-/3-}$ redox couple (+ 0.36 V vs. SHE). The selectivity of $H_2O_2$ can be calculated according to following equation:

$$\% H_2O_2 = 200 * \frac{\frac{i_{ring}}{N}}{\frac{i_{ring}}{N} + i_{disk}}$$

where $i_{ring}$ is the ring current, $i_{disk}$ is the disk current, and N is the collection efficiency (0.2245).

Chronoamperometry (CA) measurements were carried out under the above-mentioned RDE setup at 0.7 V vs. RHE for 1 h, obtaining a current-time (*i*-t) curve. CVs were taken before and after the CA holds to quantify the change in activity and cross-reference with other RDE results.

**2.5 Online ICP-MS Measurements**

Inductively coupled plasma-mass spectrometry (ICP-MS) measurements were conducted with a Thermo Scientific iCAP RQ instrument using a crossflow cell (Basi MF-1093) with a 0.5 mil gasket (Basi MF-1044). A crossflow electrode block (MF-1000) with dual embedded glassy carbon disks (area = 0.07 $cm^2$ each) was used for the working electrode and the counter electrode. A leakless Ag/AgCl electrode (MF-2056) was used as reference and was calibrated to ~0.955 V vs. RHE. $O_2$-saturated 0.1 M KOH electrolyte was flowed through the cell at 2 mL/min into the PEEK Mira Mist nebulizer using an external Ismatec peristaltic pump via 0.76 mm Viton tubing. The 2 mL/min flowrate was chosen to match ORR current densities under RDE settings (**Section 2.4**), with a 20 mV/s scan rate. To convert the ICP-MS intensity signals to concentration (ppb), standard solutions of Co, Ni, and Cu were diluted using 0.1 M KOH solution into concentrations of 0 (electrolyte blank, 0.1 M KOH), 1, 2.5, 5, 7.5, 10 and 25 ppb and measured under the same flow cell setup. A matrix-matched external standard calibration curve with a linear fitting was used to obtain concentration. The blank error range (ng/s) is obtained via the fitted linear model using the blank intensity mean plus 5 standard deviations (5σ rule, > 99.5% confidence interval). The spikes were filtered out using a similar 5σ threshold, where σ is the lower standard deviation amongst the trials and an element-based parameter. The theoretical metal loading used

to normalize the dissolved metals from online ICP-MS is calculated by the following equation:

$$\text{Theoretical Metal Loading (M1 or M2)} = \text{Ink Concentration } (\frac{mg}{cm^2}) \times \text{Electrode Geometric Area } (cm^2) \times \text{M1 or M2 Atomic Content}_{\text{pre-electrochemistry XPS}} (\%)$$

### 2.6 General Computational Details

Spin-polarized density functional theory calculations were conducted using implicit solvation of VASPsol[32] (default settings) implemented in the Vienna ab initio simulation package (VASP)[33,34] and project augmented wave (PAW) pseudopotential.[35] All calculations were performed and analyzed using the atomic simulation environment (ASE).[36] The electronic exchange and correlation energy were described using the Perdew-Burke-Ernzerhof functional.[37] In all calculations, the cutoff energy of the plane-wave basis set was 500 eV. The DFT+*U* value of 3.32, 6.45, and 3.0 eV was applied to Co, Ni and Cu using their oxide and SAC references for all the calculations.[38–42] The DFT-D3 correction was also considered in all calculations to describe the vdW-dispersion energy between the MOF layers.[43] The bulk structures of MOF were fully optimized using a dense K-point sampling mesh. The surface calculations were performed by considering three layers (3L) of MOF, where the bottom two layers were constrained. We considered a 15 Å vacuum gap to avoid interaction between periodically repeated slabs. A dipole correction was applied to reduce the interactions between the periodically repeated slabs. The surface structures were optimized using a 2×2×1 Monkhorst–Pack grid k-point. The convergence criteria of the electronic self-consistency loop were set to be $10^{-6}$ eV and 0.02 eV/Å for energy and force respectively. Crystal Orbital Hamilton Population (COHP) and integrated COHP (ICOHP) values were obtained from M-N bonds using the Lobster package,[44] and Density of State (DOS) and projected DOS (PDOS) calculations were performed using relax the electronic structure with the symmetry disabled and denser the k-point grid of 5 × 5 × 1.

### 2.7 Activity and Selectivity Calculations

The activity and selectivity of ORR process were calculated and compared between M1 (nodes) and M2 (linkers) sites for different bimetallic combinations of MOF. The

catalytic activity and selectivity were predicted by calculating the thermodynamic overpotential and the potential-determining step in the four-electron associative ORR mechanism with *OOH, *O, and *OH intermediates (**Table S1**).[45] The thermodynamic overpotential (is defined as the maximum free energy difference among all the intermediates participating ORR process and the limiting potential ($U_L$) is the highest applied potential at which all four steps are downhill in free energy i.e., overpotential = 1.23 V - $U_L$. Based on the different binding energies of adsorbates, we constructed 2D volcano heatmap indicating catalytic activity and selectivity. The free energies for each ORR steps were calculated using the computational hydrogen electrode method with zero-point energy (ZPE), vibration energy and entropy correction.[26] The vibrational enthalpy and entropy contributions were obtained by the quantum mechanical harmonic approximation at room temperature. For the ORR intermediates reference energy, we considered $H_2O$ (l) and $H_2$ (g), as PBE-DFT calculations are unable to describe the energy of $O_2$ in the gas phase accurately. The optimized MOF bulk and surface structures along with their respective total and adsorption energies are tabulated in **Table S1** and are also available online at Catalysis-hub.org[46] under https://www.catalysis-hub.org/publications/WeiTuning2024.

### 2.8 Stability Calculations

We used a similar metal dissolution mechanism to calculate dissolution during the ORR process from M-$N_4$ moiety embedded on graphene as developed by Holby et al.[47] and Hansen et. al.[48] During dissolution, the metals from both M1 and M2 site are leached out and formed an aqueous solution of $M(OH)_3^-$ at alkaline environment (pH 13) and applied potential of 0.7 V vs. RHE, observed in the Pourbaix diagram.[49] Depending on the binding energy, the resultant MOFs after M1 or M2 dissolution are protonated with various degrees. Finally, the stability of MOFs for various bimetallic combinations were estimated and tabulated in **Table S2** by computing the dissolution free energy at pH 13 and applied potential of 0.7 V vs. RHE.

## 3. Results and Discussion

### 3.1 Structural Characterization and Theoretical Validation of Dual Site MOFs

The metal (Co/Ni/Cu, II) 2,3,9,10,16,17,23,24-octaamino-phthalocyanine ligands carry a singular M-$N_4$ site, in which the N atoms originate from pyrrole nitrogens. Through the square-planar coordination of the amino groups with transition metals (metal nodes, also Co/Ni/Cu), the ligands are converted to 2D phthalocyanine-based MOFs with square lattices. This square-planar coordination was found to enable excellent electron delocalization through continuous conjugation and long-range electron conductivity in the MOFs.[29] The metal nodes in these 2D MOFs provide a different type of M-$N_4$ sites from the ligands, in which the N atoms are from two amino radicals (-$NH^{\cdot}$) and two azanides (-$NH^{-}$). Typically, metal nodes are more flexible due to the presence of smaller amino/azanides moiety as compared to bulk phthalocyanine in metal ligands. We will designate the metal node as the M1 site and the metal in the ligand as the M2 site throughout this work (**Figure 1a)**. This bimetallic feature with dual M-$N_4$ sites is particularly interesting for oxygen reduction electrocatalysis and provides a platform for tuning the performance of these MOF catalysts.

For ease of discussion, we consider Co-based MOFs to indicate MOFs that contain Co, regardless of its site. We define pure MOF when same element occupied in both M1 and M2 sites. We also consider Co-Cu to indicate M1-M2 MOF (e.g., Co is M1 and Cu is M2) while Co/Cu denotes no site specificity (e.g., is both Co-Cu and Cu-Co). X is used to imply a vacant site (X-Co means the Co precursor M2, with no M1) while Co-M2 indicates all 3 MOFs with Co as M1 (Co-Co, Co-Ni and Co-Cu). This terminology applies to all metal combinations herein (**Table S3**). No interchange of metals between sites is assumed, as in each metal is only in one site (M1 or M2).[50,51]

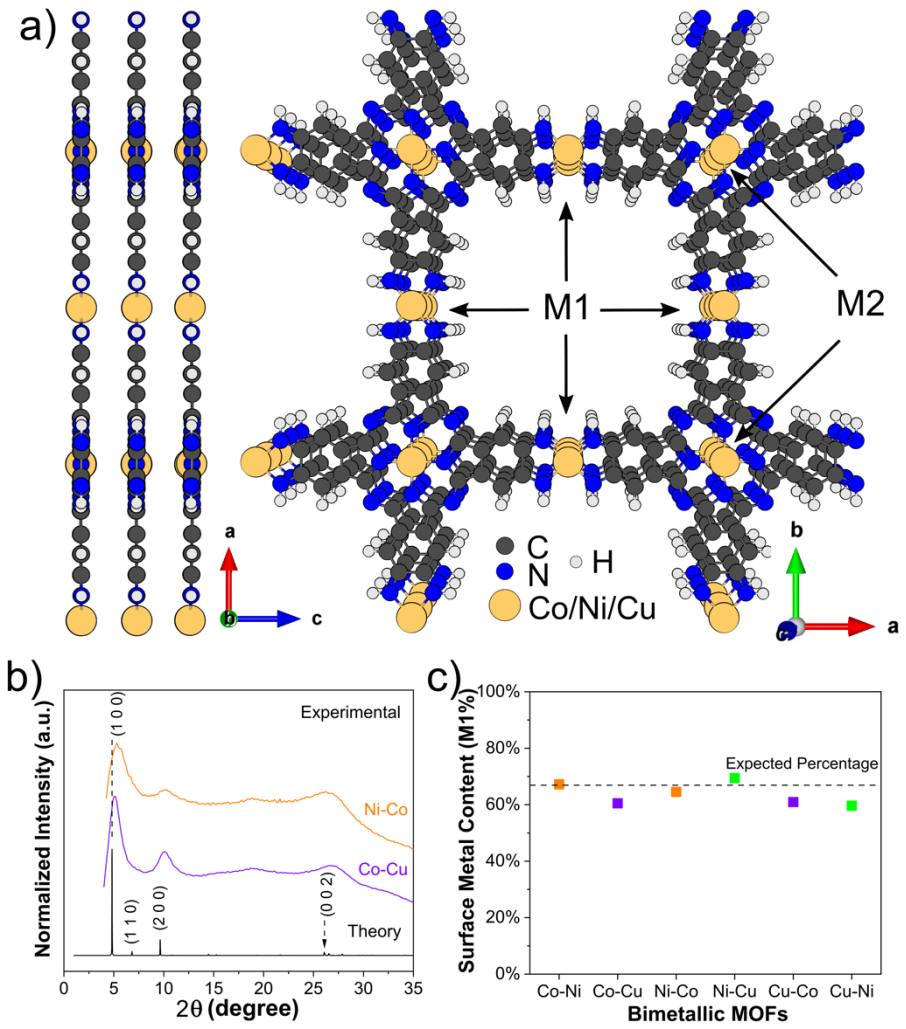


**Figure 1: Structural validation via a combined experimental and theoretical approach on representative MOFs.** a) Side and top view of the MOF structure model; b) Overlaid XRD patterns of experimentally measured Ni-Co, Co-Cu and calculated Co-Cu MOF pattern; c) Surface metal content (M1%) on as-synthesized bimetallic MOFs obtained from XPS. The dashed line indicates the expected M1 percentage of 66% (2:1 ratio). The MOFs (M1-M2) are colored using primary color mixing rules based on their metal sites (Co/Ni = orange, Co/Cu = purple, Ni/Cu = green).

**Figure 1a** shows the side and top view of the 2D-layered MOF structural model. An AA-eclipsed stacking model is used for the 2D MOF layers, as is suggested in our previous work.[29] The phthalocyanine-based ligand (with a metal site in the center, M2) and a metal node (M1) can be clearly seen from the model, with each metal site coordinated with four nitrogen atoms (M-$N_4$ structure). Structurally, M2 sites are electron poor and less covalently bonded with neighboring nitrogens than the M1 sites. The bulk Co-Co MOF structure was computationally optimized using partial (8-16 H/bulk) and full (20H/bulk) coverage of hydrogen at the ligands and we found that

structure with 16 H coverage predicts a minimum energy under ORR conditions (**Figure S1**). We also found that both sites show low spin state regardless of different hydrogen coverage. The calculated lattice parameters for bulk MOFs (pure and mixed) are summarized in **Figure S2** and tabulated in **Table S4**. We have calculated that the Co-Co system has the largest inter-layer spacing of 3.38 Å, followed by 3.32 and 3.27 Å for Ni-Ni and Cu-Cu, respectively. For mixed systems, the layer distance is controlled by the M1 sites due to their higher overall ratio and planar flexibility. **Figure 1b** shows the experimental XRD patterns for Ni-Co and Co-Cu, which are in good agreement with the general simulated XRD pattern (represented by Co-Cu). Computationally, we simulated all possible pure and mixed bulk MOFs and found almost identical peak alignments. From a structure perspective, the MOFs have strong peaks at 2θ = ~5 deg (100), ~9 deg (200), and ~27 deg (002). Our calculated and experimentally observed patterns are in alignment with our previous work,[29] although these MOFs are isostructural with the interlayer stacking distance (d-spacing) being slightly different (in the range of 3.2 to 3.4 Å) as a function of metal combination within the MOFs. Given the findings above, we have constructed surface models by considering 3 layers of 2D MOF sheet using optimized bulk MOF structures with three different inter-layer spacings (see **Table S4**) and allow only the top layer to fully relax.

Previously reported TEM images of as-synthesized Co-Cu MOF indicate a tetragonal unit cell with square pores side length of ~ 1.8 nm.[29] The Brunauer-Emmett-Teller (BET) surface areas of the MOFs are in the range of 119 (Co-Co) – 548 (Co-Cu) $m^2 g^{-1}$, suggesting decent crystallinity and porosity.[29] There are differences in the crystallinity of the MOF family, as their crystal domain sizes vary from 7.4 to 12.3 nm (excluding Co-Co). Co-Co is an amorphous MOF material (no ordered crystallites).[29] **Figure 1c** shows the surface metal content in M1% on as-synthesized bimetallic MOF powders. The M1% are within the range of 60 – 70%, close to the expected ratio of 66%. XPS fittings (**Figure S3** and **S4**) on the precursors (M2 only, X-Co/Ni/Cu) and selected MOFs suggest minor changes in binding energy for X-Ni and X-Co when M1 sites are introduced (before electrochemistry, **Figure S3b, d,** and **Figure S4d,** top two panels). Changes in X-Cu are more prominent (**Figure S4b,** top two panels), as we also confirmed much shorter d-spacing when M1 = Cu computationally (as discussed in **Figure 1, S2**). This implies that adding a secondary metal (as M1 nodes) impacts the

chemical nature of the original M2 site in the transition from the molecular precursor to a MOF which induces complex electronic and structural modifications as is discussed next.

## 3.2 Comparison on Experimental and Theoretical Performance of Dual Site MOFs

### *3.2.1 Experimental Activity and Selectivity of Dual Site MOFs*

In order to understand how metal sites can affect the activity and the selectivity of the ORR, all MOFs and precursors were tested in a standard RDE and RRDE setup (**Section 2.4**). **Figure 2a** and **2b** show the RRDE scans of Co-based MOFs in an Ar-subtracted $O_2$-saturated 0.1 M KOH solution. Ni- and Cu-based MOF scans can be found in **Figure S5**. All tested MOFs show typical ORR sigmoidal polarization curves on the disk with some hysteresis. Th mass-transport limited current density is between ~ -3.5 to -5.5 mA $cm^{-2}$ for all MOFs, while the precursors have a maximum current ~ -3 mA $cm^{-2}$ with no significant plateau. The lower disk and ring current for the precursors suggest that max current is a combination of transport, kinetics, and selectivity. CV scans in an Ar-saturated 0.1 M KOH solution show that all MOFs and precursors have slightly different profiles as a function of composition and metal site (**Figure S6**). Note that Ni and Cu precursors show possible redox feature at around 0.8 V vs. RHE (**Figure S6b, S6f**) while a redox feature is observed at around 0.6 V vs. RHE for the Co precursor (**Figure S6d**). Redox features are largely suppressed in corresponding MOFs, relative to their precursor, which could be due to the MOF structure impacting the M2 oxidation. It is interesting to note that MOFs with the highest and the lowest BET surface area, Co-Cu and Co-Co respectively,[29] exhibit similar profiles under Ar-saturated conditions which could indicate similar double layer capacitance (**Figure S6c**). This suggests that the electrochemically available surface area is different from the surface area accessible *ex-situ* by nitrogen adsorption in their powder form and is likely dominated by the Vulcan carbon in electrochemical conditions.

Similarly, conductivity and level of crystallinity do not seem to determine performance. Ni-Ni and Co-Co demonstrate the highest and lowest conductivity and level of crystallinity based on FWHM, (Ni-Ni: conductivity = 54.3 mS $cm^{-1}$, crystallite size =

12.3 nm vs. Co-Co: conductivity = $8.9\times10^{-4}$ mS $cm^{-1}$, amorphous),[29] respectively, yet as we will discuss below, they have similar performance with moderate current densities at 0.7 V vs. RHE. Therefore, while material properties such as gas adsorption surface area, crystallinity, conductivity, etc. can affect the total electrochemical performance of MOFs, our data indicates that these trends do not coincide with activity trends. Thus, our data suggests that the metal site and composition of these MOFs could play a dominating role in activity. Moving forward, we will discuss in-depth the intricacies of these metal sites, while also acknowledging the minor influences from the above-mentioned parameters.

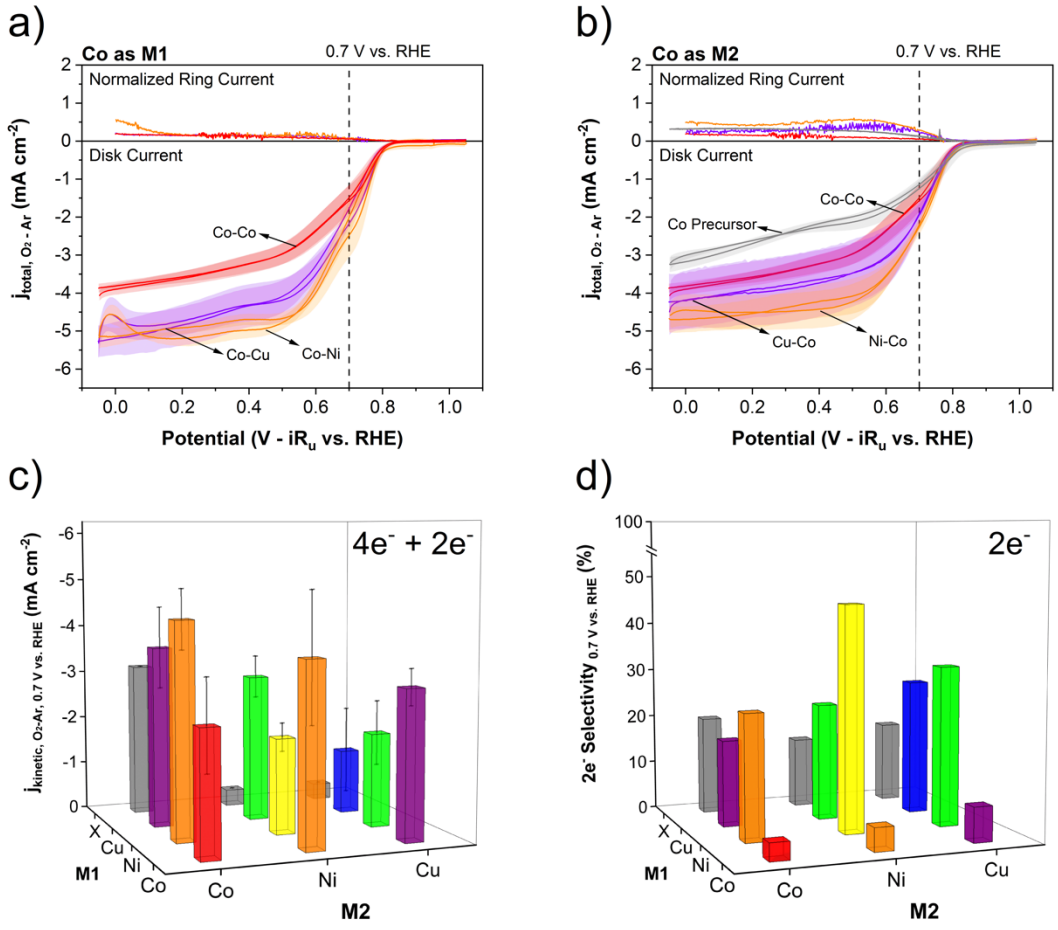


**Figure 2**: **Activity and selectivity analysis on MOFs (M1-M2) and precursors (X-M2)**. Rotating ring disk electrode (RRDE) cyclic voltammograms (j-V) from 0 V to 1 V vs. RHE on MOFs using a) Co as M1; b) Co as M2, including the Co precursor; Top panel: normalized ring current with a collection efficiency N = 0.2245; Bottom panel: disk current. Three-dimensional bar graphs on c) kinetic current density and d) two-electron selectivity at 0.7 V vs. RHE in $O_2$-saturated 0.1 M KOH solution (background subtracted with that in Ar-saturated 0.1 M KOH solution). Scan rate: 20 mV/s, rotation rate: 1600 rpm. The MOFs (M1-M2) are colored using primary color mixing rules based on their metal sites (Co = red, Ni = yellow, Cu = blue, Co/Ni = orange, Co/Cu = purple, Ni/Cu = green). The precursors (X-M2) are

colored grey (X indicates a vacant M1 site). All potentials are on a reversible hydrogen electrode (RHE) scale and are 85% $iR_u$ compensated.

**Figure 2c** shows the kinetic current density on all 9 MOFs (M1-M2) and 3 precursors (X-M2) at 0.7 V vs. RHE on a 3-D bar graph. On average, comparison of current density indicates that metal combinations, regardless of site location, play a large role in activity with Co/Ni (orange) catalysts showing a ~1.2 higher current density than Co/Cu (purple) and both demonstrating 1.2 – 1.5-fold higher current density than Co-Co (red), respectively (**Table S3**). Generally, Co-based MOFs have higher performance, with Ni-Co having the highest kinetic current density of all ($j_{kin,\ Ni\text{-}Co}$ = -4.4 mA $cm^{-2}$). Co is a promising ORR element as the Co precursor (X-Co) exhibits approximately 9 times higher current density than that of the Ni and Cu precursors ($j_{kin,\ X\text{-}Co} \sim 9 \times j_{kin,\ X\text{-}Ni} \sim 9 \times j_{kin,\ X\text{-}Cu}$).[29] Despite X-Ni and X-Cu having the lowest kinetic current densities of the catalysts tested, MOFs with Ni as M2 and Cu as M2 can increase up to ~11-fold in activity compared to the corresponding precursor. This could be due to adding more accessible active sites to the system and/or building a framework structure. It was previously shown that analogous Co-based MOFs have lower crystallinity than Ni/Cu, Ni-Ni, and Cu-Cu.[29] The low crystallinity of Co-Co combined with X-Co and Co-Co having similar performance (e.g., Co-Co), could indicate why Ni/Cu combinations are more sensitive to the MOF structure.

**Figure 2d** summarizes the two-electron selectivity for all MOFs with respect to their precursors. Comparing these compositions, all catalysts with low two-electron selectivity have Co as M1 (Co-M2 < ~ 8%), while Cu as M1 has moderate two-electron selectivity (Cu-M2 ~ 18% - 28% and Ni as M1 has high two-electron selectivity (Ni-M2 ~ 25% - 46%, **Table S3**). Note that despite differences in selectivity the partial four-electron kinetic current density exhibits similar trends to the total current density (**Figure 2c, d**), suggesting that the four-electron ORR pathway is dominant. The selectivity trends could suggest that $H_2O_2$ production is dominated by M1 sites, with minor variations as a function of the M2 site. This observed trend is in agreement with Co being a four-electron selective element and Ni a two-electron selective element and further supported by Co-Co having the lowest two-electron selectivity (~ 4%) and Ni-Ni having the highest (~ 46%) with the largest $H_2O_2$ current amongst all MOFs (**Figure**

**S5d**). From a structural perspective, M1 sites are known to be more electron rich than M2 sites, which can weaken the binding strength of $H_2O_2$ at metal centers and facilitate the two-electron ORR pathway for selective production of $H_2O_2$.[45] We provide more detailed analysis of this effect in the next section. Altogether, our experimental results indicate that while there are slight differences in physical properties of the MOFs, MOF structure and composition, Co incorporation plays the largest role in tuning the total current density for ORR and selectivity. To probe the relative differences of MOF composition, active site-specific atomistic calculations are necessary.

### *3.2.2 Predicted Activity and Selectivity of Dual Site MOFs*

The advantage of studying multi-site MOFs is a greater active site tunability, however, experimentally, distinguishing the individual role of these active sites is complicated. To distinguish the role that each metal site plays in activity, we perform the computational screening of the activity of the M1 and M2 sites using surface models of MOFs (discussed in **Section 3.1**). The theoretical limiting potentials are calculated as the largest steps of the direct four-electron pathway or a partial two-electron pathway (**Equations 1, 2**). We obtain binding energies of *OOH, *O, and *OH adsorbates on both M1 and M2 sites for nine bimetallic combinations evaluated experimentally (see Methods **Section 2.7**). For all calculations, we consider implicit solvation (VASPsol) in our model to capture the effects of aqueous environment during the ORR process (see **Methods Section 2.6**).

The predicted ORR activity of M1 and M2 sites for different MOFs are presented in **Figure 3.** The ORR volcano plot (**Figure 3a**) shows the limiting potential ($U_L$) as OH* activity descriptor for four-electron ORR process. The inset in **Figure 3a shows** the optimized surface structure of MOF indicating on-top OH* binding on both M1 and M2 sites embedded in M-$N_4$ as described above. The parallel dashed line corresponding to 0.7 V represents the equilibrium potential for two-electron ORR process, while the vertical dashed line indicates the region of four-electron (left side) vs two-electron (right side) selectivity for ORR process as reference to Au (111).[7]

The key finding from **Figure 3a** is that Co-based MOFs, regardless of M1 or M2 site, are positioned at top of the volcano plot, indicating higher ORR activity and a preference selectivity for four-electron ORR, followed by Cu- and Ni-based MOFs. Co-

based MOF outperformed other bimetallic MOF might be attributed to the favorable redox potential ($Co^{2+}/Co^{3+}$) which facilitates the formation of active intermediates (OH*/OOH*) involved in the ORR. Overall, M2 sites exhibit more dominant ORR activity compared to M1 sites. To investigate the activity differences between M1 and M2 sites, and their origin, we conduct PDOS and ICOHP analysis for pure MOFs (Co-Co, Cu-Cu, Ni-Ni) (see Method **Section 2.6**). The binding strength is function of available bonding, which is directly measured by OH adsorption. For octahedral metal-oxides systems,[52] as we had shown previously, that binding strength directly correlates with -ICOHP. Our ICOHP analysis unveils site-specific activity differences rather than element-specific ones. Regardless of various pure MOFs, we consistently observe that the M2 site has a higher d-band center (and a less negative ICOHP value) compared to the M1 site (refer to **Table S5 and Figure S7**). This indicates less saturated M-N bonding at M2 sites, resulting in overall stronger OH adsorption. Beyond these electronic effects, we also identified the propensity of M1 sites to off-planar flex to be much greater than M2 with an extended pyrrole nitrogen's network. These structural effects have important implications on the activity of mixed bimetallic systems.

In our study of various mixed bimetallic systems, we found that most of the M2 sites, especially Co as M2 site, show a high selectivity for the four-electron ORR process. Conversely, most M1 sites, particularly Ni, exhibit weaker *OOH binding energy, making them more selective for the two-electron ORR process. These findings are in excellent agreement with experimental observations. Further, we compare the activity of Co at M2 site for different M1 sites (Co, Cu, and Ni). The limiting potential volcano plot in **Figure 3a** shows the activity trends are as follows: Ni-Co > Cu-Co > Co-Co. We found that the effects of different elements at M1 sites on the activity of M2 sites (Co) are both electronic and geometric, arising from local strain as we discuss next.

To evaluate the electronic effect of M1 site on M2 site activity, we calculate the OH* binding energy of Co (M2) site for Ni-Co system with or without Ni (having $Ca^{2+}$) in the M1 site (**Figure S8**). Here, we found almost ~0.4 eV differences in the OH* adsorption energy on the M2 (Co) site for with Ni as opposed to the case without Ni (having $Ca^{2+}$) in M1 sites, suggesting that electronic effects of M1 site on M2 site activity are significant. Furthermore, we observed that the activity of the Co (M2) site in a layered system further increases under internal stress, which arises from the varying

inter-layer distances between Co vs. Ni and Cu based MOFs. As we discussed earlier (see **Section 3.1** and in **Figure 1a**), M1 sites are more prevalent (2:1 ratio) and thus play a dominant role in controlling the overall MOF layer structure. Hence for the Ni-Co system, the top Ni (M1) moves closer to the second layer Ni (M1), which results in a non-planar concave (convex) shape in M2-N4 (M1-N4) moiety and thus boosting the activity (indicated by arrows in **Figure 3a**). We found that the larger the concave angle (between M1-M2), the stronger is the OH* binding energy (see **Figure S9**), which is well supported by the recent literature regarding the binding of CO on distorted cobalt phthalocyanine (CoPc).[53] Our result revealed that among three different M1 sites (Cu, Ni, Co), the Cu as M1 site shows the highest (~175º vs 180º) concave angle at M2-N4 sites and therefore resulting strongest OH* adsorption. In terms of trends, the optimum OH* binding is seen on Co (M2) in the Ni-Co pair, predicting the highest four-electron ORR activity among all studied MOF systems. The 2D volcano (shown in **Figure S10**) plot indicates that the Co as M2 site in the Ni-Co bimetallic combination predicts a minimum overpotential of 0.27 V due to near optimal OOH*-OH* value, exhibiting the highest ORR activity among all pairs studied, in good agreement with experimental results.

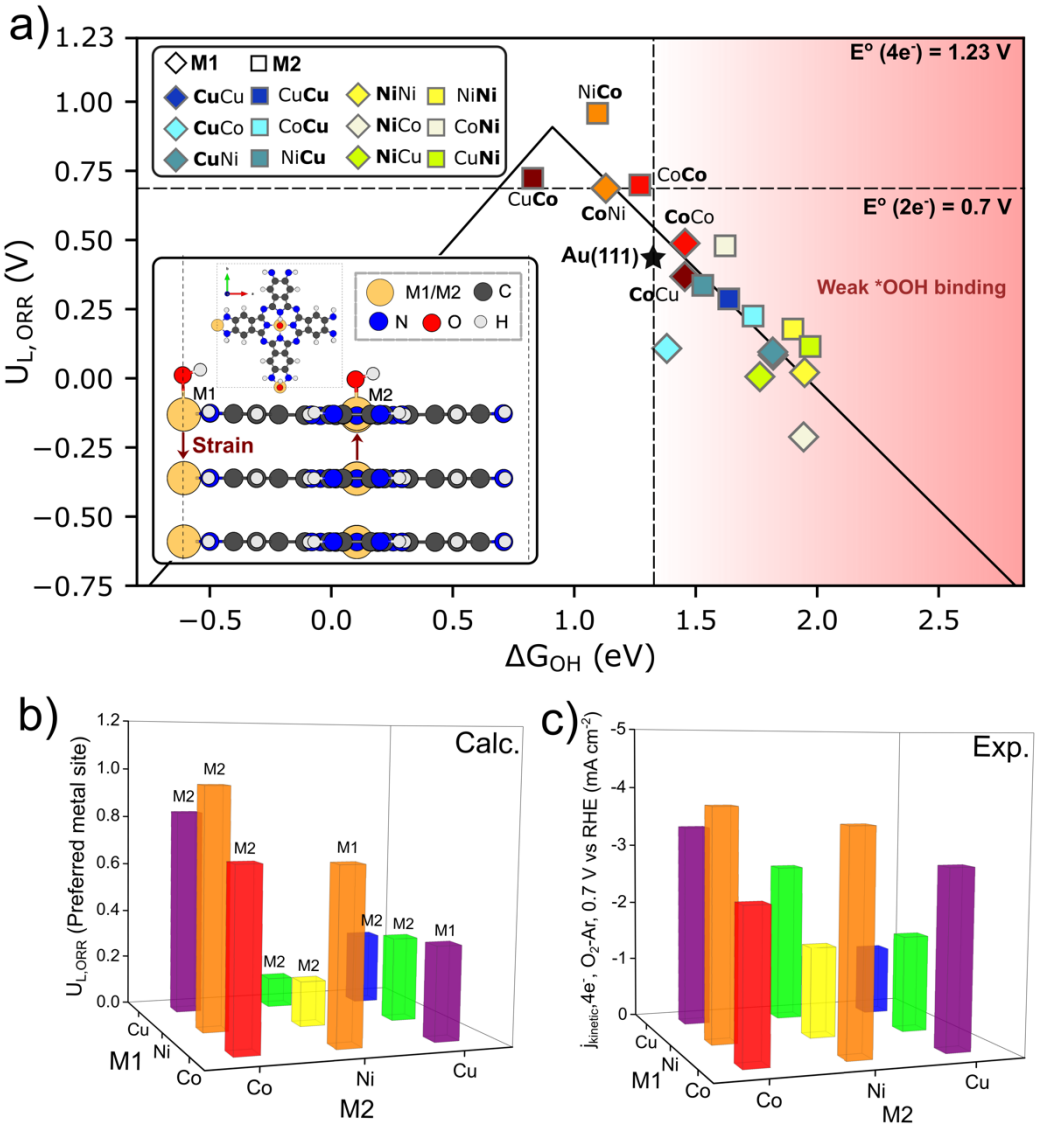


**Figure 3. Computational model of MOF and their predicted selectivity and activity for ORR.** a) Volcano plot for ORR process indicates limiting potential of MOF (each site) towards four-electron ORR for flat layers. The color gradient indicates weaker *OOH binding regions (two-electron selective). Inset figure indicates the theory model for 3 layers of MOF indicating adsorbed OH* on two metal nodes (M1) and one organic linker (M2) site. Arrows in inset figure indicate point of strain for mixed MOF systems, which results concave (convex) at M2 (M1) site, see also **Figure S9**. b) Bar plot showing the predicted limiting potential for higher ORR activity site between the M1 and M2 of MOF. c) Bar plot represents the partial current density for four-electron ORR process at 0.7 V vs. RHE (data from **Figure 2c** and **2d**).

**Figures 3b and 3c** show the side-by-side comparison between the theoretically predicted thermodynamic limiting potentials ($U_L$) and experimentally measured current densities for four-electron ORR process at 0.7 V vs. RHE. **Figure 3b** represents the limiting potential for the higher ORR activity site between the M1/M2 of MOF. Our calculations indicate that Co has a higher limiting potential, indicating better ORR activity, regardless of whether it is the M1 or the M2 site. For the other non-Co

bimetallic MOFs, M2 sites show higher 4-electron activity than M1 sites regardless of type of metal. The experimental results show that Co-containing MOFs have the highest current densities (**Figure 3c**), which is strongly supported by the theory prediction. Moreover, the pairs without Co such as Ni-Cu and Cu-Ni show minimal ORR activity, where M2 sites are also dominate in activity. The linear trend between current density for four-electron ORR process at 0.7 V vs. RHE and theory predicted overpotential, is also observed in **Figure S11.**

Overall, there is substantial agreement between the computational predictions and experimental measurements regarding trends in activity and selectivity. This is notable given the relative straightforwardness of the model, without adding significant complexity, e.g. explicit electrolyte effects beyond simple solvation, catalyst dynamics and degradation, and other effects. Additionally, the choice of the DFT+*U* value for Cu and Ni, along with the challenge of modeling different oxidation state of Cu, may arise certain variations specifically Cu-Ni (with Cu at the M1 site), in which the measured performance was much higher than that predicted by theory, suggesting opportunities to further explore these materials to better understand the nature of the active site and surrounding microenvironment. Despite not capturing all possible effects, however, the general agreement between the computational results and the experimental measurements indicates that Co is highly active as either the M1 or the M2 site, dictating the ORR activity, whereas in the absence of Co, the activity is controlled by the M2 site. The majority of the M1 sites are more selective for two-electron ORR. Building on this understanding of the factors that govern activity and selectivity, we note that complex materials as MOFs require assessment of structural transformations or instabilities such as dissolution during electrochemistry; these are factors that we directly address next.

### 3.3 Electrochemical and Theoretical Dual Site MOF Material Stability Evaluation

#### *3.3.1 Experimental Evaluation of Stability*

MOFs have been shown to evolve during testing and are often considered pre-catalysts in many oxidative electrochemical environments (e.g., OER).[54,55] The identification of degradation mechanisms within selected applied potential ranges of stability could suggest possible strategies to address instability, guide the design of next-generation

materials, and contribute to the broader knowledge base. When evaluating the 1 h electrochemical performance of the high-performing Co-based MOFs at 0.7 V vs. RHE, CA measurements indicate that all tested MOFs exhibit noticeable activity degradation (**Figure S12**). However, the performance degradation in some cases was recoverable (See SI note for **Figure S12**), suggesting a dynamic active site. As performance deterioration can be attributed to many aspects of material degradation including pore structure change, metal leaching, support interactions, etc., it is critical to analyze the mechanisms of material degradation within a short time frame before diving into broader long-term performance evaluation.

This is particularly relevant for the MOF electrochemical community, as the complexity of this class of materials challenges the development of methodologies for assessing the dynamics of the catalyst during electrochemical evaluation. This challenge has presented itself in studies of MOF catalysts for the OER where massive bulk degradation is expected, in part, due to carbon corrosion.[54,55] During ORR, however, where carbon species are more stable, more subtle degradation is expected. The level of structural decomposition (e.g., loss of MOF network) and chemical composition changes (e.g., leaching of M1/M2 metals) of the MOFs catalysts during ORR could shed light on whether the MOF structure plays a role in activity or if the MOF template provides a pre-catalyst template for an active yet disordered M-N-C catalyst. Unfortunately, determining the *in-situ*/*operando* structural integrity is difficult as it may or may not be related to metal dissolution (M1 or M2), N removal, change in electrochemical surface area, change in diffraction pattern, etc. Within these limitations we have focused our attempts to understand the dynamics of our MOF structure using composition-focused techniques, e.g., ICP-MS and XPS. We believe that the change in M1:M2 ratios can give insight into specific active sites but may not necessarily relate to MOF structural evolution.

To develop mechanisms for material stability, we focused on Co-based bimetallic MOFs in a short time-period (3 CV cycles) for optimal chemical-time resolution. Online ICP-MS flow cell studies were performed to quantify the loss of metals and to probe possible degradation pathways (see **Methods Section 2.5**).

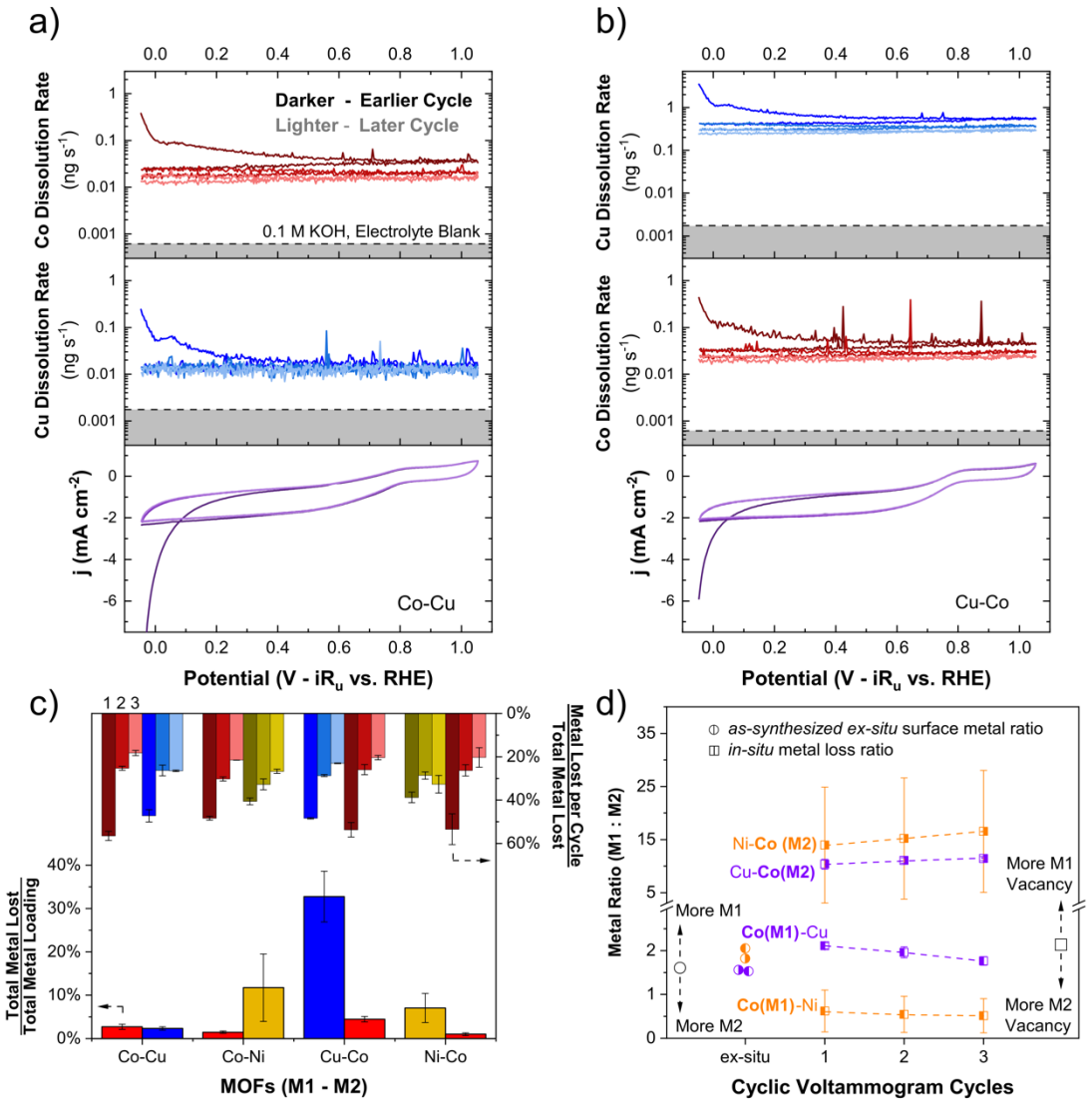


**Figure 4: Stability analysis on Co-based bimetallic MOFs via online inductively coupled plasma - mass spectrometry (online ICP - MS).** Three panel line graphs of dissolution rates for a) Co-Cu; b) Cu-Co measured over 3 CV cycles from 0 to 1 V vs. RHE where darker shades indicate earlier cycles. Top panel: M1 dissolution rate (semi-log graph); Middle panel: M2 dissolution rate (semi-log graph); Bottom panel: current density – potential (j-V) CV scans in $O_2$-saturated 0.1 M KOH solution. Shaded grey area indicates the +5σ measurement error range on the electrolyte blank (0.1 M KOH) for Co, Ni, and Cu (See Section 2.5 for details); c) Left-Y: Total metal dissolution (%) over 3 CV cycles comparing dissolved metals from entire online ICP-MS to theoretical loading calculated from XPS ratios (See Section 2.5 for details); Right-Y: Cycle breakdown on the metal dissolution (%) for each metal (Co = red, Ni = yellow, Cu = blue, left: M1 site, right: M2 site); d) *ex-situ* pre-electrochemistry surface metal ratios from XPS (circles, M1:M2, close to the expected ratio of 2, where higher M1:M2 ratio means more M1 sites on the surface) and *in-situ* metal loss ratios from online ICP-MS (squares, CV cycles 1-3, showing the ratios of metals lost during flowcell electrochemistry where higher M1:M2 ratio means more M1 losses from the bulk and the surface, resulting in more M1 vacancies in the framework) on Co-based bimetallic MOFs. All potentials are on a reversible hydrogen electrode (RHE) scale and are 85% $iR_u$ compensated. Error bars are based on duplicate samples.

**Figure 4a** and **4b** show the dissolution rate (ng/s) of Cu and Co for Co/Cu MOFs as a function of potential during three standard CVs (**Figure S13a** and **S13b** for Co/Ni MOFs). The apparent current density trend amongst the 4 measured MOFs measured *via* online ICP-MS (**Figure S14**) is in good agreement with that measured *via* RDE (**Figure 2c**), suggesting good translation of these MOFs across different techniques. The current density measured *via* online ICP-MS is lower, likely due to different mass transport in the RDE cell at 1,600 rpm vs. the flow cell at 2 mL $min^{-1}$. Generally, the dissolution profiles of Co-based bimetallic MOFs (**Figure 4a**, **4b, S13)** show some combination of three distinct features: 1) random loss not due to dissolution (spikes), 2) initial high dissolution rate that decreases after the first cycle, and 3) constant baseline dissolution (positive dissolution rates). Since the spikes appear to be quite random and only account for less than 1 wt.% of the total metal loss, they were filtered out of the data for ease of discussion. It is unclear why these spikes were observed as many factors such as bubbles, nanoparticle formation, artifacts of the experiment, etc. can cause spikes that are above the baseline noise.

For all Co and Cu dissolutions, there is an initial decay of dissolution rate (**Figure 4a and b**, less prominent in Ni, **Figure S13**) that coincides with a ramp in current seen immediately upon the application of a potential to the system at the beginning of electrochemical testing (bottom panel). Such decay could be due to the initial dissolution of defect sites (e.g., edge sites) and/or the disruption/re-balance of the metal-ligand coordination from open circuit potential (OCV) to under potential. This sharp decay also contributes strongly to the total metal dissolution, as the majority of the dissolution for Co, Cu, and Ni (largely in M1 position), happens in cycle 1 for all tested Co-based bimetallic MOFs (right y-axis of **Figure 4c).** While most of the dissolution happens in cycle 1, the dissolution rates across all cycles and total dissolution trends are largely the same. It is interesting to note that the baseline dissolution within our testing window does not exhibit a strong dependence on potential or current density, suggesting that neither catalysis nor material redox events are driving dissolution. This is consistent with small dissolution always being present a low concentration of metals in solution.[56]

To account for the total (no spikes) metal loss over 3 cycles, a dissolution rate to time integration was performed on both metals for the Co-based bimetallic MOFs and

normalized respectively to the total loading of each metal, as is shown in the left y-axis of **Figure 4c**. The non-normalized total net dissolution amount (ng) can be found in **Figure S15**. Broadly, Co leaches less than Ni and Cu, suggesting that Co is a more stable element during ORR. Assuming all MOF sites are initially pristine, both Co and Ni exhibit no significant site dependence in their dissolution, but Cu exhibits a very strong site dependence, with far more loss (~ 14-fold) when at M1 site (Cu-Co) (**Figure 4a and b**). It is important to note that the differences in the metal/site dissolution trends can suggest different degradation pathways for these Co-based bimetallic MOFs. Given the framework structure of these MOFs, the loss of M2 sites can lead to vacancies in the ligand center whereas the loss of M1 sites could lead to more losses in M2 as nanoparticles and/or potential structural degradation (back to its precursor). For the Cu-Co case specifically, the loss of Cu from the structure did not appear to impact the ORR performance. This is consistent with the calculations that the Co site is dominant in the Cu-Co MOF, but does not clarify experimentally, if the MOF structure is required for the Co activity. Therefore, while most of the catalysts tested are largely stable to dissolution, in the future it would be necessary to find a characterization handle that allows for monitoring both the metal dissolution ratio during ORR and the structural evolution of MOF catalysts.

**Figure 4d** shows the surface and bulk metal ratios for all Co-based bimetallic MOFs. The *ex-situ* metal ratios are surface atomic ratios measured by XPS on as-synthesized powder samples (pre-electrochemistry, **Figure 1c**). The cycles 1-3 metal ratios are *in-situ* metal loss ratios from the bulk catalytic film, calculated from the online ICP-MS experiments (**Figure S16**). Under electrochemical testing (cycles 1 to 3), the majority of ratio changes happen in cycle 1 for all tested MOFs, which could be due to the initial potential application, after which the ratio remains relatively stable. Moreover, the changes in metal ratios can be grouped into three categories based on the position of Co. When Co is at M2 site (Ni-Co and Cu-Co), there is a high M1:M2 loss ratio, suggesting more M1 site metal (node) loss from the bulk during electrochemistry. If the porous network is dependent on the coordination from the M1 site, then a high M1:M2 loss ratio would be consistent with degrading the MOFs back to its precursor (X-Co) and loss of the MOF structure. When Co is at the M1 site, the loss ratio is dependent on the M2 composition. For Co-Cu the loss ratio is nominally the same as the expected

2:1 ratio, suggesting stoichiometric loss of material (stoichiometric dissolution rate). On the other hand, Co-Ni has a low M1:M2 loss ratio suggesting that more vacancies are created in the center of the ligand, possibly preserving some of the framework structure. Amongst these tested MOFs, Co-Cu serves as the most probable catalyst that preserved its MOF structure during electrochemical testing, as its M1:M2 loss ratio remained constant and close to the theoretical value throughout the experiment. Although, again, the loss of the M1 does not necessarily mean that the MOF structure is not maintained. New characterization methods would need to be developed to address this point explicitly. Thus, the degradation pathway of these MOFs is preferentially dependent on the placement of Co, as Co is much more stable than Ni and Cu, followed by the M2 composition.

To further complement the above-discussed online ICP-MS studies and understand the chemical nature of the catalysts, predominantly the metals, *ex-situ* TEM and XPS were conducted on the Co-based bimetallic MOFs that underwent 8 standard CV cycles of RDE testing and compared with that taken on the precursors and pre-electrochemistry samples. (**Figure S3, S4, bottom panels, S17**). As was shown previously,[29] the crystal domains of as-synthesized Co-Cu, Ni-Co MOFs are ca. 10 nm, however, the MOF motifs in the post-electrochemistry catalysts **(Figure S17)** are difficult to distinguish as they are embedded in a Vulcan carbon and Nafion network. Note that due to the strong overlap with $F_{KLL}$ in the Ni-*2p* region and up to ~40% of metal loss, the post-electrochemistry metal ratios are less reliable. Furthermore, small shifts in binding energy and changes in peak shapes take place after electrochemical testing, suggesting changes in local environment and/or electronic structure **(Figure S3-S4)**.

*3.3.2. MOF Stability Calculations*

To elucidate the experimentally measured stability of M1/M2 sites under ORR conditions for four Co-containing bimetallic pairs (Co-Cu, Co-Ni, Ni-Co, Cu-Co), we have computationally studied the dissolution behavior of MOFs. **Figure 5** illustrate the schematic representation of the dissolution process for the M1 and M2 sites from the MOF structure under alkaline ORR conditions (pH 13 and potential 0.7 V vs. RHE). We found that pristine MOFs (adsorbate-free) are energetically more stable compared to systems with adsorbates (see **Figure S18)** and are directly used to the study of

dissolution process (shown as **Figure 5a**). Under these conditions, the metal atoms (M1 or M2) convert into an aqueous hydroxide solution, specifically $M(OH)_3^-$ was identified as the terminal phase from the experimental Pourbaix diagrams of Co, Ni, Cu metals at room temperature of 298 K and a metal ion concentration of $10^{-6}$ M.[49,57,58] The resulting metal cavity in the MOF structure is then further protonated as reported previously[48] (see **Figure S19**).

**Figure 5b and 5c** present the top view of the surface layer and the side view of MOF layers, after the formation of M1 and M2 cavities. In **Figure 5b**, the leaching of the M1 site (note that we only consider one of the two M1 sites for calculation) results in the formation of stable 4-($NH_2$) ligands, causing a slight distortion from their original geometry. Conversely, no significant distortion is observed after the M2 site dissolution and formation of 2-(NH) ligands, as shown in **Figure 5c**. The overall trend in the magnitude of distortion caused by the dissolution of M1 sites is Cu > Ni > Co. The possible dissolution reactions of MOF (M-$N_4$) under ORR conditions are as follows:

For M1 site dissolution:

$$(M1 - N_4C) + 4H_2O + 2e^- \leftrightarrow M1(OH)_3^- + H_4N_4C + OH^- \qquad (3)$$

For M2 site dissolution:

$$(M2 - N_4C) + 2H_2O \; + \; OH^- \leftrightarrow M2(OH)_3^- + H_2N_4C \qquad (4)$$

Using Equations (3, 4), we can now directly calculate the free energy difference, $\Delta G_{diss}$ $\left(G_{product} - G_{reactant}\right)$, between the products and reactants, which we define as the descriptor of metal dissolution for MOF. Higher values of $\Delta G_{diss}$ indicate lower stability of the MOF under ORR conditions and vice versa.

**Figures 5d, 5e** represent a side-by-side comparison between the calculated dissolution descriptor and experimentally measured metal dissolution (normalized) rate, respectively. In **Figure 5d,** it is found that in all pairs except Co-Ni, Co exhibits a lower free energy of dissolution than the other metal, indicating that Co is the most stable element in MOFs. On the other hand, among all studied elements, Cu as M1 shows a larger value, indicating it to be the least stable metal in the MOFs. The trend of stability for M1 sites are Co>Ni>Cu, which further supported by our ICOHP trends (**see Table**

**S5**). Additionally, as previously discussed (**see Table S4 and Figure S9**), the tendency of Cu and Ni as M1s site to shorten the inter-layer distances, along with their effects on MOF geometry and activity, may further contribute to their lower stability. Similarly, we observed a trend in the M2 site stability, with Co>Ni>Cu, moreover, Co as M2 in Ni-Co pairs exhibits the lowest dissolution, indicating that it is the most stable element in MOFs during ORR operating conditions. Our experimental measurements show that Co leaches the least compared to other elements (**Figure 5e**). Among all measured Co-based MOFs, Cu as M1 in Cu-Co is the least stable element and Co as M2 site in Ni-Co is the most stable, demonstrating excellent agreement with calculated dissolution descriptor for the stability study of MOFs under ORR operating conditions.

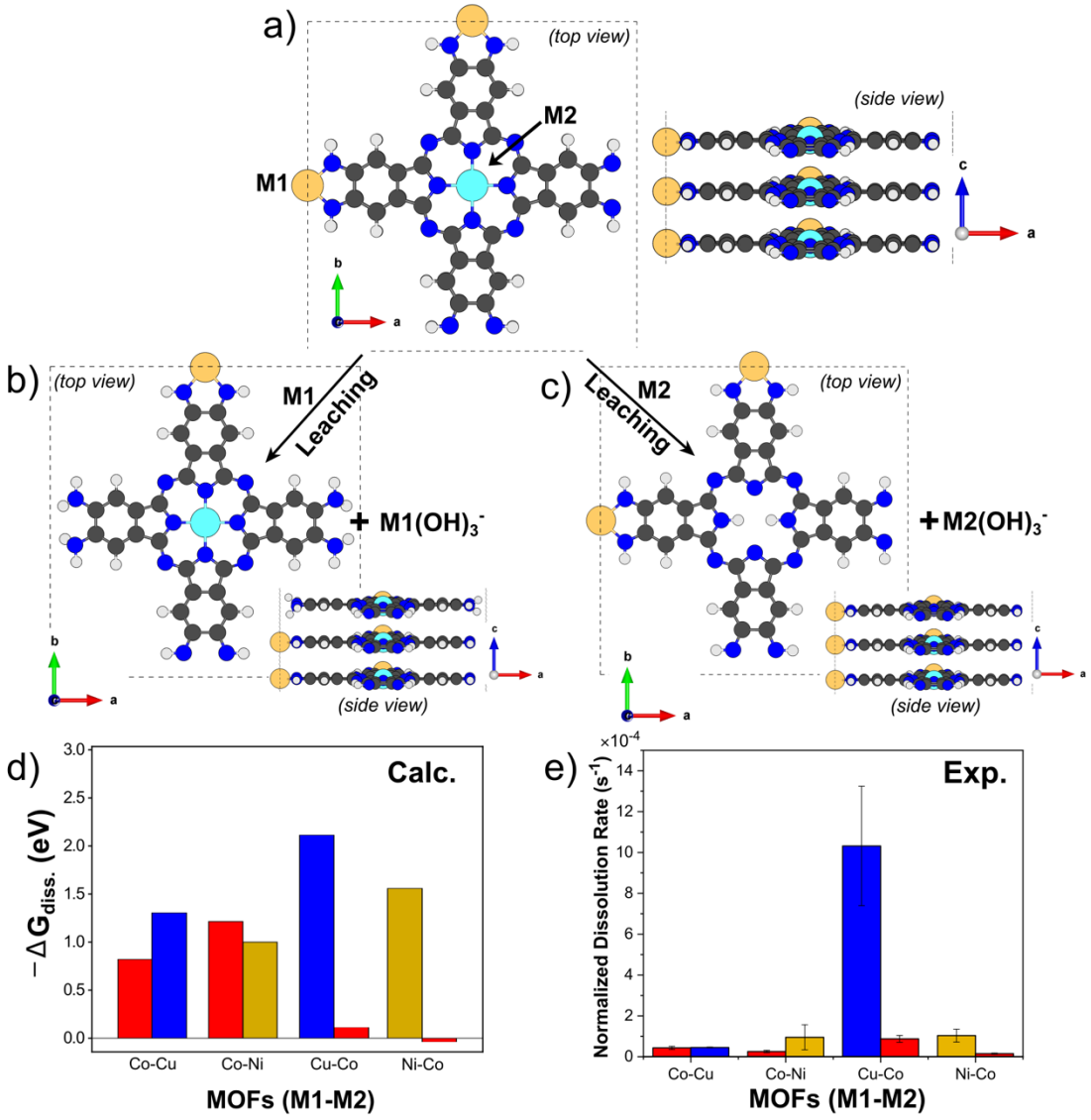

**Figure 5. Theoretically predicted metal dissolution mechanism and thermodynamic stability of MOFs under alkaline conditions.** a) Pristine MOF model before electrochemical study. The resulting MOF structure containing metal cavity after M1 (b), and M2 (c) sites leach into solution as $M1/M2(OH)_3^-$. d) Calculated free energy changes between the products and the reactant as a descriptor of metal dissolution for MOFs at metal ion concentration of $10^{-6}$ M, and e) Experimentally measured metals dissolution rate (normalized) under ORR conditions (pH 13 and applied potential 0.7 vs. RHE).

## 4. Conclusions

By exploring MOFs with dual transition metal centers (M-$N_4$ moieties, M1-M2, where M=Co, Ni, Cu), we have established a clear correlation between adsorbate bonding on the metals and their corresponding catalytic activity, selectivity, and material durability when driving the ORR under alkaline conditions. Drawing on insights from both experimental and theoretical studies, our results reveal that Co-based MOFs, in particular Ni-Co, demonstrate the highest kinetic activity for ORR among all nine MOFs. Our theoretical modeling underscores the pivotal role of Co-active sites and identifies the less saturated M2-$N_4$ bonds leading to the dominance of the M2 site over the M1 site. In mixed metal MOFs, M1 nodes consisting of Cu or Ni enforce shorter inter-layer distances, compelling the linkers to form a non-planar, concave-like shape at the M2 (Co) sites, further activating the M2-$N_4$ moiety and thus enhancing the ORR activity. We further demonstrate that the M1 sites can greatly impact the catalyst selectivity, as shown by the cases of Co and Ni in the M1 sites dramatically steering the catalyst towards four-electron and two-electron selectivity, respectively. In-situ measurements of material stability allowed for a quantitative measurement of dissolution from both metal sites during ORR, which was found to be relatively constant throughout the experiment. Computationally, we studied MOF dissolution mechanisms under alkaline ORR conditions and calculated the free energy as a descriptor of metal dissolution. Both calculated and measured dissolution indicate that Co is the most stable element regardless of site. Moreover, substantial dissolution of Cu at the M1 site was also observed, possibly due to the tendency of a shorter inter-layer distance and the associated structural stress. Overall, a very good agreement between experimental data and calculated results for activity, selectivity and stability validate of the combined theory-experimental approach to study the MOFs for ORR. Future work could include testing and comparison in acidic media where more degradation is expected, and mechanistic insights could be valuable in designing more

stable materials. Furthermore, this study highlights the importance of M2 sites moving forward as well as new directions for improving the performance further by tuning the strain of the metal sites. These findings provide guidance for the development of MOFs with tailored electrocatalytic properties, offering opportunities for non-precious metal catalysts in emerging energy applications.

## Acknowledgments

This work was supported the U.S. Department of Energy, Office of Science, Office of Basic Energy Sciences, Chemical Sciences, Geosciences, and Biosciences Division, Catalysis Science Program, to the SUNCAT Center for Interface Science and Catalysis. Part of this work was performed at the Stanford Nano Shared Facilities (SNSF) and the Stanford Nanofabrication Facility (SNF), supported by the National Science Foundation under Award ECCS-2026822. This research used resources of the National Energy Research Scientific Computing Center, a DOE Office of Science User Facility supported by the Office of Science of the U.S. Department of Energy under Contract No. DE-AC02-05CH11231 using NERSC award BES-ERCAP0024127.

## Supporting Information

Further information on detailed experimental data such as XPS fittings and TEM images on the pre- and post-electrochemistry MOFs, RDE (CVs and CAs) and RRDE scans under different conditions, and theoretical calculations (DFT + U correction, adsorption sites, stability, overpotentials, free energies for activity and stability). All optimized structure and their corresponding free energies are found at https://www.catalysis-hub.org/publications/WeiTuning2024.

## References


(1) Aminudin, M. A.; Kamarudin, S. K.; Lim, B. H.; Majilan, E. H.; Masdar, M. S.; Shaari, N. An Overview: Current Progress on Hydrogen Fuel Cell Vehicles. *Int. J. Hydrogen Energy* **2023**, *48* (11), 4371–4388. https://doi.org/10.1016/j.ijhydene.2022.10.156.

(2) Manoharan, Y.; Hosseini, S. E.; Butler, B.; Alzhahrani, H.; Senior, B. T. F.; Ashuri, T.; Krohn, J. Hydrogen Fuel Cell Vehicles; Current Status and Future Prospect. *Appl. Sci.* **2019**, *9* (11), 2296. https://doi.org/10.3390/app9112296.

(3) Midilli, A.; Dincer, I. Key Strategies of Hydrogen Energy Systems for Sustainability. *Int. J. Hydrogen Energy* **2007**, *32* (5), 511–524. https://doi.org/10.1016/J.IJHYDENE.2006.06.050.

(4) Saeedmanesh, A.; Mac Kinnon, M. A.; Brouwer, J. Hydrogen Is Essential for Sustainability. *Curr. Opin. Electrochem.* **2018**, *12*, 166–181. https://doi.org/10.1016/J.COELEC.2018.11.009.

(5) Firouzjaie, H. A.; Mustain, W. E. Catalytic Advantages, Challenges, and Priorities in Alkaline Membrane Fuel Cells. *ACS Catal.* **2020**, *10* (1), 225–234. https://doi.org/10.1021/ACSCATAL.9B03892.

(6) Stevens, M. B.; Anand, M.; Kreider, M. E.; Price, E. K.; Zeledón, J. Z.; Wang, L.; Peng, J.; Li, H.; Gregoire, J. M.; Hummelshøj, J.; Jaramillo, T. F.; Jia, H.; Nørskov, J. K.; Roman-Leshkov, Y.; Shao-Horn, Y.; Storey, B. D.; Suram, S. K.; Torrisi, S. B.; Montoya, J. H. New Challenges in Oxygen Reduction Catalysis: A Consortium Retrospective to Inform Future Research. *Energy Environ. Sci.* **2022**, *15* (9), 3775–3794. https://doi.org/10.1039/D2EE01333A.

(7) Kulkarni, A.; Siahrostami, S.; Patel, A.; Nørskov, J. K. Understanding Catalytic Activity Trends in the Oxygen Reduction Reaction. *Chem. Rev.* **2018**, *118* (5), 2302–2312. https://doi.org/10.1021/ACS.CHEMREV.7B00488/ASSET/IMAGES/LARGE/CR-2017-00488T_0008.JPEG.

(8) Kelly, S. R.; Kirk, C.; Chan, K.; Nørskov, J. K. Electric Field Effects in Oxygen Reduction Kinetics: Rationalizing Ph Dependence at the Pt(111), Au(111), and Au(100) Electrodes. *AIChE Annu. Meet. Conf. Proc.* **2020**, *2020-November*, 14581–14591. https://doi.org/10.1021/ACS.JPCC.0C02127/ASSET/IMAGES/LARGE/JP0C02127_0006.JPEG.

(9) Ma, R.; Lin, G.; Zhou, Y.; Liu, Q.; Zhang, T.; Shan, G.; Yang, M.; Wang, J. A Review of Oxygen Reduction Mechanisms for Metal-Free Carbon-Based Electrocatalysts. *npj Comput. Mater. 2019 51* **2019**, *5* (1), 1–15. https://doi.org/10.1038/S41524-019-0210-3.

(10) Seh, Z. W.; Kibsgaard, J.; Dickens, C. F.; Chorkendorff, I.; Nørskov, J. K.; Jaramillo, T. F. Combining Theory and Experiment in Electrocatalysis: Insights into Materials Design. *Science (80-. ).* **2017**, *355* (6321), eaad4998. https://doi.org/10.1126/science.aad4998.

(11) Burkitt, R.; Whiffen, T. R.; Yu, E. H. Iron Phthalocyanine and MnOx Composite Catalysts for Microbial Fuel Cell Applications. *Appl. Catal. B Environ.* **2016**, *181*, 279–288. https://doi.org/10.1016/J.APCATB.2015.07.010.

(12) Tylus, U.; Jia, Q.; Strickland, K.; Ramaswamy, N.; Serov, A.; Atanassov, P.; Mukerjee, S. Elucidating Oxygen Reduction Active Sites in Pyrolyzed Metal-Nitrogen Coordinated Non-Precious-Metal Electrocatalyst Systems. *J. Phys. Chem. C* **2014**, *118* (17), 8999–9008. https://doi.org/10.1021/jp500781v.

(13) Sgarbi, R.; Kumar, K.; Jaouen, F.; Zitolo, A.; Ticianelli, E. A.; Maillard, F. Oxygen Reduction Reaction Mechanism and Kinetics on M-NxCy and M@N-C Active Sites Present in Model M-N-C Catalysts under Alkaline and Acidic Conditions. *J. Solid State Electrochem.* **2021**, *25* (1), 45–56. https://doi.org/10.1007/s10008-019-04436-w.

(14) Han, J.; Bao, H.; Wang, J. Q.; Zheng, L.; Sun, S.; Wang, Z. L.; Sun, C. 3D N-Doped Ordered Mesoporous Carbon Supported Single-Atom Fe-N-C Catalysts with Superior Performance for Oxygen Reduction Reaction and Zinc-Air

Battery. *Appl. Catal. B Environ.* **2021**, *280* (August 2020), 119411. https://doi.org/10.1016/j.apcatb.2020.119411.

(15) Zhong, H.; Ly, K. H.; Wang, M.; Krupskaya, Y.; Han, X.; Zhang, J.; Zhang, J.; Kataev, V.; Büchner, B.; Weidinger, I. M.; Kaskel, S.; Liu, P.; Chen, M.; Dong, R.; Feng, X. A Phthalocyanine-Based Layered Two-Dimensional Conjugated Metal–Organic Framework as a Highly Efficient Electrocatalyst for the Oxygen Reduction Reaction. *Angew. Chemie* **2019**, *131* (31), 10787–10792. https://doi.org/10.1002/ange.201907002.

(16) Barkholtz, H. M.; Liu, D. J. Advancements in Rationally Designed PGM-Free Fuel Cell Catalysts Derived from Metal-Organic Frameworks. *Mater. Horizons* **2017**, *4* (1), 20–37. https://doi.org/10.1039/c6mh00344c.

(17) Jahan, M.; Liu, Z.; Loh, K. P. A Graphene Oxide and Copper-Centered Metal Organic Framework Composite as a Tri-Functional Catalyst for HER, OER, and ORR. *Adv. Funct. Mater.* **2013**, *23* (43), 5363–5372. https://doi.org/10.1002/adfm.201300510.

(18) Lu, X. F.; Xia, B. Y.; Zang, S.-Q.; Lou, X. W. (David). Metal–Organic Frameworks Based Electrocatalysts for the Oxygen Reduction Reaction. *Angew. Chemie* **2020**, *132* (12), 4662–4678. https://doi.org/10.1002/ANGE.201910309.

(19) Sen, R.; Saha, D.; Koner, S.; Brandão, P.; Lin, Z. Single Crystal to Single Crystal (SC-to-SC) Transformation from a Nonporous to Porous Metal-Organic Framework and Its Application Potential in Gas Adsorption and Suzuki Coupling Reaction through Postmodification. *Chem. - A Eur. J.* **2015**, *21* (15), 5962–5971. https://doi.org/10.1002/chem.201405684.

(20) Song, B. Y.; Li, M. J.; Yang, Y. W.; He, Y. L. Achievement of a Novel Porous Non-Noble-Metal Catalyst with Excellent Oxygen Reduction Reaction Activity: Promoting the Commercialization of Alkaline Fuel Cells. *J. Clean. Prod.* **2020**, *249*, 119314. https://doi.org/10.1016/J.JCLEPRO.2019.119314.

(21) Maity, K.; Karan, C. K.; Biradha, K. Porous Metal-Organic Polyhedral Framework Containing Cuboctahedron Cages as SBUs with High Affinity for

H2 and CO2 Sorption: A Heterogeneous Catalyst for Chemical Fixation of CO2. *Chem. - A Eur. J.* **2018**, *24* (43), 10988–10993. https://doi.org/10.1002/chem.201802829.

(22) Zagal, J. H.; Bedioui, F. Electrochemistry of N4 Macrocyclic Metal Complexes. Springer Cham **2016**.

(23) De Oteyza, D. G.; El-Sayed, A.; Garcia-Lastra, J. M.; Goiri, E.; Krauss, T. N.; Turak, A.; Barrena, E.; Dosch, H.; Zegenhagen, J.; Rubio, A.; Wakayama, Y.; Ortega, J. E. Copper-Phthalocyanine Based Metal-Organic Interfaces: The Effect of Fluorination, the Substrate, and Its Symmetry. *J. Chem. Phys.* **2010**, *133* (21), 4703. https://doi.org/10.1063/1.3509394.

(24) Zagal, J.; Pgez, M.; Tanaka, A. A.; Santos, J. R. Dos; Linkous, C. A. Electrocatalytic Activity of Metal Phthalocyanines for Oxygen Reduction *. *J. Ekctroanal Chem* **1992**, *339*, 13–30.

(25) Yuan, S.; Peng, J.; Zhang, Y.; Zheng, D. J.; Bagi, S.; Wang, T.; Román-Leshkov, Y.; Shao-Horn, Y. Tuning the Catalytic Activity of Fe-Phthalocyanine-Based Catalysts for the Oxygen Reduction Reaction by Ligand Functionalization. *ACS Catal.* **2022**, *12* (12), 7278–7287. https://doi.org/10.1021/ACSCATAL.2C00184/ASSET/IMAGES/LARGE/CS2C00184_0007.JPEG.

(26) Nørskov, J. K.; Rossmeisl, J.; Logadottir, A.; Lindqvist, L.; Kitchin, J. R.; Bligaard, T.; Jónsson, H. Origin of the Overpotential for Oxygen Reduction at a Fuel-Cell Cathode. *J. Phys. Chem. B* **2004**, *108* (46), 17886–17892. https://doi.org/10.1021/JP047349J/ASSET/IMAGES/LARGE/JP047349JF00008.JPEG.

(27) Viswanathan, V.; Hansen, H. A.; Rossmeisl, J.; Nørskov, J. K. Universality in Oxygen Reduction Electrocatalysis on Metal Surfaces. *ACS Catal.* **2012**, *2* (8), 1654–1660. https://doi.org/10.1021/CS300227S/SUPPL_FILE/CS300227S_SI_001.PDF.

(28) Zheng, W.; Lee, L. Y. S. Metal-Organic Frameworks for Electrocatalysis:

Catalyst or Precatalyst? *ACS Energy Letters*. American Chemical Society August 13, 2021, pp 2838–2843. https://doi.org/10.1021/acsenergylett.1c01350.

(29) Chen, G.; Li, Z.; Huang, Z.; Lu, H.; Long, G.; Lezama Pacheco, J. S.; Tok, J. B. H.; Gao, T. Z.; Lei, Y.; Zhou, J.; Bao, Z. Effects of Transition Metals on Metal-Octaaminophthalocyanine-Based 2D Metal-Organic Frameworks. *ACS Nano* **2023**, *17* (10), 9611–9621. https://doi.org/10.1021/acsnano.3c03143.

(30) Fairley, N.; Fernandez, V.; Richard-Plouet, M.; Guillot-Deudon, C.; Walton, J.; Smith, E.; Flahaut, D.; Greiner, M.; Biesinger, M.; Tougaard, S.; Morgan, D.; Baltrusaitis, J. Systematic and Collaborative Approach to Problem Solving Using X-Ray Photoelectron Spectroscopy. *Appl. Surf. Sci. Adv.* **2021**, *5* (May), 100112. https://doi.org/10.1016/j.apsadv.2021.100112.

(31) Kreider, M. E.; Kamat, G. A.; Zamora Zeledón, J. A.; Wei, L.; Sokaras, D.; Gallo, A.; Stevens, M. B.; Jaramillo, T. F. Understanding the Stability of Manganese Chromium Antimonate Electrocatalysts through Multimodal In Situ and Operando Measurements. *J. Am. Chem. Soc.* **2022**, *144* (49), 22549–22561. https://doi.org/10.1021/jacs.2c08600.

(32) Mathew, K.; Sundararaman, R.; Letchworth-Weaver, K.; Arias, T. A.; Hennig, R. G. Implicit Solvation Model for Density-Functional Study of Nanocrystal Surfaces and Reaction Pathways. *J. Chem. Phys.* **2014**, *140* (8), 4106. https://doi.org/10.1063/1.4865107/1003843.

(33) Kresse, G.; Furthmüller, J. Efficient Iterative Schemes for *Ab Initio* Total-Energy Calculations Using a Plane-Wave Basis Set. *Phys. Rev. B* **1996**, *54* (16), 11169. https://doi.org/10.1103/PhysRevB.54.11169.

(34) Kresse, G.; Furthmüller, J. Efficiency of Ab-Initio Total Energy Calculations for Metals and Semiconductors Using a Plane-Wave Basis Set. *Comput. Mater. Sci.* **1996**, *6* (1), 15–50. https://doi.org/10.1016/0927-0256(96)00008-0.

(35) Blöchl, P. E. Projector Augmented-Wave Method. *Phys. Rev. B* **1994**, *50* (24), 17953. https://doi.org/10.1103/PhysRevB.50.17953.

(36) Hjorth Larsen, A.; JØrgen Mortensen, J.; Blomqvist, J.; Castelli, I. E.; Christensen, R.; Dułak, M.; Friis, J.; Groves, M. N.; Hammer, B.; Hargus, C.; Hermes, E. D.; Jennings, P. C.; Bjerre Jensen, P.; Kermode, J.; Kitchin, J. R.; Leonhard Kolsbjerg, E.; Kubal, J.; Kaasbjerg, K.; Lysgaard, S.; Bergmann Maronsson, J.; Maxson, T.; Olsen, T.; Pastewka, L.; Peterson, A.; Rostgaard, C.; SchiØtz, J.; Schütt, O.; Strange, M.; Thygesen, K. S.; Vegge, T.; Vilhelmsen, L.; Walter, M.; Zeng, Z.; Jacobsen, K. W. The Atomic Simulation Environment—a Python Library for Working with Atoms. *J. Phys. Condens. Matter* **2017**, *29* (27), 273002. https://doi.org/10.1088/1361-648X/AA680E.

(37) Perdew, J. P.; Burke, K.; Ernzerhof, M. Generalized Gradient Approximation Made Simple [Phys. Rev. Lett. 77, 3865 (1996)]. *Phys. Rev. Lett.* **1997**, *78* (7), 1396. https://doi.org/10.1103/PhysRevLett.78.1396.

(38) Jiang, S.; Mushrif, S. H. Determining Surface-Specific Hubbard-U Corrections and Identifying Key Adsorbates on Nickel and Cobalt Oxide Catalyst Surfaces. *Phys. Chem. Chem. Phys.* **2023**, *25* (12), 8903–8912. https://doi.org/10.1039/D2CP04814K.

(39) Moore, G. C.; Horton, M. K.; Linscott, E.; Ganose, A. M.; Siron, M.; O'Regan, D. D.; Persson, K. A. High-Throughput Determination of Hubbard U and Hund J Values for Transition Metal Oxides via the Linear Response Formalism. *Phys. Rev. Mater.* **2024**, *8* (1), 4409. https://doi.org/10.1103/PhysRevMaterials.8.014409.

(40) Jain, A.; Hautier, G.; Ong, S. P.; Moore, C. J.; Fischer, C. C.; Persson, K. A.; Ceder, G. Formation Enthalpies by Mixing GGA and GGA + U Calculations. *Phys. Rev. B - Condens. Matter Mater. Phys.* **2011**, *84* (4), 5115. https://doi.org/10.1103/PhysRevB.84.045115.

(41) Wang, L.; Maxisch, T.; Ceder, G. Oxidation Energies of Transition Metal Oxides within the GGA+U Framework. *Phys. Rev. B - Condens. Matter Mater. Phys.* **2006**, *73* (19), 5107. https://doi.org/10.1103/PhysRevB.73.195107.

(42) Duan, Z.; Henkelman, G. Surface Charge and Electrostatic Spin Crossover

Effects in CoN4Electrocatalysts. *ACS Catal.* **2020**, *10* (20), 12148–12155. https://doi.org/10.1021/acscatal.0c02458.

(43) Grimme, S.; Antony, J.; Ehrlich, S.; Krieg, H. A Consistent and Accurate Ab Initio Parametrization of Density Functional Dispersion Correction (DFT-D) for the 94 Elements H-Pu. *J. Chem. Phys.* **2010**, *132* (15), 4104. https://doi.org/10.1063/1.3382344/926936.

(44) Maintz, S.; Deringer, V. L.; Tchougréeff, A. L.; Dronskowski, R. LOBSTER: A Tool to Extract Chemical Bonding from Plane-Wave Based DFT. *J. Comput. Chem.* **2016**, *37* (11), 1030–1035. https://doi.org/10.1002/jcc.24300.

(45) Hansen, H. A.; Viswanathan, V.; NØrskov, J. K. Unifying Kinetic and Thermodynamic Analysis of 2 E- and 4 e - Reduction of Oxygen on Metal Surfaces. *J. Phys. Chem. C* **2014**, *118* (13), 6706–6718. https://doi.org/10.1021/JP4100608/SUPPL_FILE/JP4100608_SI_001.PDF.

(46) Winther, K. T.; Hoffmann, M. J.; Boes, J. R.; Mamun, O.; Bajdich, M.; Bligaard, T. Catalysis-Hub.Org, an Open Electronic Structure Database for Surface Reactions. *Sci. Data* **2019**, *6* (1), 75. https://doi.org/10.1038/s41597-019-0081-y.

(47) Holby, E. F.; Wang, G.; Zelenay, P. Acid Stability and Demetalation of PGM-Free ORR Electrocatalyst Structures from Density Functional Theory: A Model for "Single-Atom Catalyst" Dissolution. *ACS Catal.* **2020**, *10* (24), 14527–14539. https://doi.org/10.1021/ACSCATAL.0C02856/ASSET/IMAGES/LARGE/CS0C02856_0007.JPEG.

(48) Hansen, H. A.; Patniboon, T. Acid-Stable and Active M−N−C Catalysts for the Oxygen Reduction Reaction: The Role of Local Structure. *ACS Catal.* **2021**, *11* (21), 13102–13118. https://doi.org/10.1021/ACSCATAL.1C02941/ASSET/IMAGES/LARGE/CS1C02941_0005.JPEG.

(49) Chivot, J.; Mendoza, L.; Mansour, C.; Pauporté, T.; Cassir, M. New Insight in

the Behaviour of Co–H2O System at 25–150 °C, Based on Revised Pourbaix Diagrams. *Corros. Sci.* **2008**, *50* (1), 62–69. https://doi.org/10.1016/J.CORSCI.2007.07.002.

(50) Liao, M. S.; Scheiner, S. Electronic Structure and Bonding in Metal Phthalocyanines, Metal=Fe, Co, Ni, Cu, Zn, Mg. *J. Chem. Phys.* **2001**, *114* (22), 9780–9791. https://doi.org/10.1063/1.1367374.

(51) Berezin, D. B.; Shukhto, O. V; Nikol, M. S.; Berezin, B. D. Some Peculiarities of Metal Exchange Reactions in Porphyrin and Phthalocyanine Complexes. *Russ. J. Coord. Chem.* **2005**, 31, 95-100. https://doi.org/10.1007/s11173-005-0028-z.

(52) Comer, B. M.; Li, J.; Abild-Pedersen, F.; Bajdich, M.; Winther, K. T. Unraveling Electronic Trends in O∗ and OH∗ Surface Adsorption in the MO2Transition-Metal Oxide Series. *J. Phys. Chem. C* **2022**, 126 (18), 7903-7909. https://doi.org/10.1021/acs.jpcc.2c02381.

(53) Su, J.; Musgrave, C. B.; Song, Y.; Huang, L.; Liu, Y.; Li, G.; Xin, Y.; Xiong, P.; Li, M. M. J.; Wu, H.; Zhu, M.; Chen, H. M.; Zhang, J.; Shen, H.; Tang, B. Z.; Robert, M.; Goddard, W. A.; Ye, R. Strain Enhances the Activity of Molecular Electrocatalysts via Carbon Nanotube Supports. *Nat. Catal.* **2023**, *6* (9), 818–828. https://doi.org/10.1038/s41929-023-01005-3.

(54) Zheng, D. J.; Görlin, M.; Mccormack, K.; Kim, J.; Peng, J.; Xu, H.; Ma, X.; Lebeau, J. M.; Fischer, R. A.; Román-Leshkov, Y.; Shao-Horn, Y. Linker-Dependent Stability of Metal-Hydroxide Organic Frameworks for Oxygen Evolution. **2023**, *30*, 46. https://doi.org/10.1021/acs.chemmater.3c00316.

(55) Ma, X.; Zheng, D. J.; Hou, S.; Mukherjee, S.; Khare, R.; Gao, G.; Ai, Q.; Garlyyev, B.; Li, W.; Koch, M.; Mink, J.; Shao-Horn, Y.; Warnan, J.; Bandarenka, A. S.; Fischer, R. A. Structure-Activity Relationships in Ni-Carboxylate-Type Metal-Organic Frameworks' Metamorphosis for the Oxygen Evolution Reaction. *ACS Catal.* **2023**, *13* (11), 7587–7596. https://doi.org/10.1021/ACSCATAL.3C00625/SUPPL_FILE/CS3C00625_SI_

001.PDF.

(56) Kan, K.; Guevarra, D.; Zhou, L.; Jones, R. J. R.; Lai, Y.; Richter, M.; Gregoire, J. M. Accelerated Characterization of Electrode-Electrolyte Equilibration. *ChemCatChem* **2023**, 16 (6), e202301300. https://doi.org/10.1002/cctc.202301300.

(57) Beverskog, B.; Puigdomenech, I. Revised Pourbaix Diagrams for Copper at 25 to 300°C. *J. Electrochem. Soc.* **1997**, *144* (10), 3476–3483. https://doi.org/10.1149/1.1838036/XML.

(58) Beverskog, B.; Puigdomenech, I. Revised Pourbaix Diagrams for Nickel at 25–300 °C. *Corros. Sci.* **1997**, *39* (5), 969–980. https://doi.org/10.1016/S0010-938X(97)00002-4.
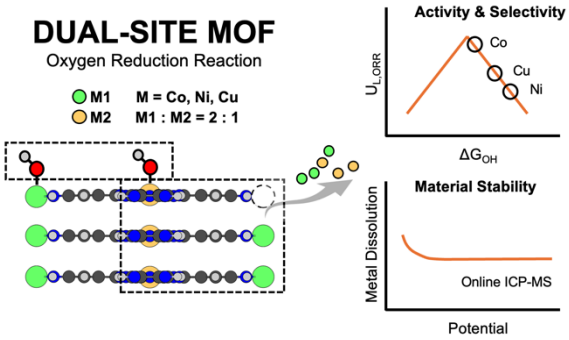
*For Table of Contents Only*